

LETTER TO THE EDITOR

# Doubly substituted isotopologues of HCCCN in TMC-1: Detection of $D^{13}CCCN$ , $DC^{13}CCN$ , $DCC^{13}CN$ , $DCCC^{15}N$ , $H^{13}C^{13}CCN$ , $H^{13}CC^{13}CN$ , $HC^{13}C^{13}CN$ , $HCC^{13}C^{15}N$ , and $HC^{13}CC^{15}N^*$

B. Tercero<sup>1,2</sup>, N. Marcelino<sup>1,2</sup>, E. Roueff<sup>3</sup>, M. Agúndez<sup>4</sup>, C. Cabezas<sup>4</sup>, R. Fuentetaja<sup>4</sup>, P. de Vicente<sup>2</sup>, and J. Cernicharo<sup>4</sup>

<sup>1</sup> Observatorio Astronómico Nacional (IGN), C/ Alfonso XII 3, 28014 Madrid, Spain

<sup>2</sup> Observatorio de Yebes (IGN). Cerro de la Palera s/n, 19141 Yebes, Guadalajara, Spain  
e-mail: b.tercero@oan.es

<sup>3</sup> LERMA, Observatoire de Paris, PSL Research University, CNRS, Sorbonne Université, 92190 Meudon, France

<sup>4</sup> Grupo de Astrofísica Molecular, Instituto de Física Fundamental, CSIC, C/ Serrano 123, 28006 Madrid, Spain  
e-mail: jose.cernicharo@csic.es

Received: 12 December 2023 / Accepted: 22 January 2024

## ABSTRACT

We report the first detection in space of a complete sample of nine doubly substituted isotopologues of HCCCN towards the cyanopolyne peak of TMC-1 using observations of the QUIJOTE<sup>1</sup> line survey taken with the Yebes 40 m telescope. We detected  $D^{13}CCCN$ ,  $DC^{13}CCN$ ,  $DCC^{13}CN$ ,  $DCCC^{15}N$ ,  $H^{13}C^{13}CCN$ ,  $H^{13}CC^{13}CN$ ,  $HC^{13}C^{13}CN$ ,  $HCC^{13}C^{15}N$ , and  $HC^{13}CC^{15}N$  through their  $J = 4 - 3$  and  $J = 5 - 4$  lines in the 7 mm window. In addition, we present an extensive analysis of the emission of HCCCN and its singly substituted isotopologues through a large velocity gradient model of the lines detected at 7 mm and 3 mm using the Yebes 40 m and the IRAM 30 m telescopes, respectively. The derived column densities for all the isotopologues are consistent in the two spectral bands for an  $H_2$  volume density of  $1 \times 10^4 \text{ cm}^{-3}$  and a kinetic temperature of 10 K. Whereas we observed a  $^{13}C$  fractionation for  $HCC^{13}CN$  and other double isotopologues with a  $^{13}C$  atom adjacent to the nitrogen atom, we derived similar  $C^{13}C$  abundance ratios for the three  $^{13}C$  substituted species of DCCCN. This suggests additional chemical discrimination for deuterated isotopologues of HCCCN. Finally, we present the spatial distribution of the  $J = 4 - 3$  and  $J = 5 - 4$  lines from the singly substituted species observed with the Yebes 40 m telescope. The emission peak of the spatial distribution of DCCCN appears to be displaced by  $\sim 40''$  with respect to that of HCCCN and the  $^{13}C$  and  $^{15}N$  isotopologues. In addition to a different formation route for the deuterated species, we could also expect that this differentiation owing to the deuterium fractionation is more efficient at low temperatures, and therefore, that deuterated species trace a colder region of the cloud.

**Key words.** Astrochemistry – ISM: abundances – ISM: clouds, TMC-1 – ISM: molecules – line: identification

## 1. Introduction

The ultra-sensitive line survey of TMC-1 with the QUIJOTE<sup>1</sup> project (Cernicharo et al. 2021b) has revealed a complex chemistry in this source, with the detection of more than 50 new molecular species (see e.g. Cernicharo et al. 2021b,a; Cabezas et al. 2022a; Agúndez et al. 2021; Cernicharo et al. 2023a, and references therein). This new approach of ultra-sensitivity,  $\sigma < 0.1 \text{ mK}$ , permits us to detect most of the molecules that are present in the cloud and allows new discoveries. However, a concern connected to this approach is related to the identification of the lines from the isotopologues of molecular species with line intensities  $\geq 30 \text{ mK}$ . This means well known molecules such as HCCCN, HCCNC, HNCCC,  $CH_3CCH$ ,  $CH_3CN$ ,  $C_4H$ ,

$C_3H$ ,  $C_3N$ ,  $C_6H$ , and many sulphur-bearing species (Cernicharo et al. 2021c, Fuentetaja et al. in prep.). Some of these species are so abundant that even doubly substituted isotopologues are expected to be present in QUIJOTE. Many of the 2500 still unidentified features in QUIJOTE arise from these isotopologues. In order to progress in the discovery of new species, we have undertaken a systematic analysis of singly and doubly substituted species of these abundant molecules.

In this Letter, we report the first identification in space of a complete and coherent sample of doubly substituted species of HCCCN, including  $D^{13}CCCN$ ,  $DC^{13}CCN$ ,  $DCC^{13}CN$ ,  $DCCC^{15}N$ ,  $H^{13}C^{13}CCN$ ,  $H^{13}CC^{13}CN$ ,  $HC^{13}C^{13}CN$ ,  $HCC^{13}C^{15}N$ , and  $HC^{13}CC^{15}N$  in the dark starless cloud TMC-1 (Sect. 3). Of these species,  $H^{13}C^{13}CCN$ ,  $H^{13}CC^{13}CN$ , and  $HC^{13}C^{13}CN$  have previously been identified in the interstellar medium (ISM) in the planetary nebula K4-47 (Schmidt & Ziurys 2019), and they were tentatively detected in the high-mass star-forming region Sgr B2 (Belloche et al. 2016). A thorough large velocity gradient (LVG) analysis of the singly and doubly substituted isotopologues of HCCCN in TMC-1 is also provided by combining the emission detected at 7 mm and 3 mm using the data achieved with the Yebes 40 m and the IRAM 30 m tele-

\* Based on observations with the Yebes 40m radio telescope (projects 19A003, 20A014, 20D023, 21A011, 21D005, 22A007, 22B029, and 23A024) and the IRAM 30m radiotelescope. The 40m radiotelescope at Yebes Observatory is operated by the Spanish Geographic Institute (IGN, Ministerio de Transportes y Movilidad Sostenible). IRAM is supported by INSU/CNRS (France), MPG (Germany), and IGN (Spain).

<sup>1</sup> Q-band Ultrasensitive Inspection Journey to the Obscure TMC-1 Environment.

scopes, respectively (Sect. 3.1). Then, reliable isotopic ratios in the region are derived (Sect. 3.2). In Sect. 4 we show the spatial distribution of the  $J = 4 - 3$  and  $J = 5 - 4$  lines from the singly substituted species observed with the Yebes 40 m telescope and discuss the results. Finally, our main conclusions are summarised in Sect. 5.

## 2. Observations

The data presented here are part of the QUIJOTE line survey performed at the Yebes 40 m radio telescope<sup>2</sup> (Cernicharo et al. 2021b, 2023a), the IRAM 30 m line survey of TMC-1 (Cernicharo et al. 2012; Marcelino et al. 2023), and the imaging-line survey SANCHO<sup>3</sup>, carried out with the Yebes 40 m telescope (Cernicharo et al. 2023b). These observations were performed towards the cyanopolyne peak (CP) position in TMC-1 at  $\alpha_{J2000} = 4^{\text{h}}41^{\text{m}}41.9^{\text{s}}$  and  $\delta_{J2000} = +25^{\circ}41'27.0''$ .

We covered the full Q band (7 mm) at the 40 m telescope, between 31.1 GHz and 50.4 GHz using the NANOCOSMOS high-electron-mobility transistor (HEMT) receiver and the fast Fourier-transform spectrometers (FFTS) with  $8 \times 2.5$  GHz bands per linear polarization, which allow a simultaneous scan with a bandwidth of 18 GHz at a spectral resolution of 38 kHz (Tercero et al. 2021). Details of the observations and data reduction were provided by Cernicharo et al. (2021b) and Cernicharo et al. (2023a). The IRAM 30 m data consist of a 3 mm line survey that covers the full available band at the IRAM 30 m telescope between 71.6 GHz and 117.6 GHz, using the EMIR 090 receiver connected to the FFTS in its narrow mode, which provides a spectral resolution of 49 kHz and a total bandwidth of 7.2 GHz. Additional details were provided by Agúndez et al. (2023) and Cernicharo et al. (2023a). Observations for the SANCHO maps were described in Cernicharo et al. (2023b). These data were recorded at the Yebes 40 m telescope using the on-the-fly mode in frequency switching with a throw of 10 MHz.

For all these data, the intensity scale in the spectra is  $T_{\text{A}}^*$ , the antenna temperature corrected for atmospheric absorption and spillover losses, which was calibrated using two absorbers at different temperatures and the atmospheric transmission model ATM (Cernicharo 1985; Pardo et al. 2001). The estimated global uncertainty for  $T_{\text{A}}^*$  is 10%. However, the relative calibration within the Q band in the line survey and in the maps is much better, and it is dominated by the statistical noise produced by the system. Pointing and focus were checked every one to two hours, and the pointing errors were within 2-3''. Details of the efficiencies and beam half-power intensities for the observations presented here are given in Table A.1. All the data were reduced and analysed using the GILDAS<sup>4</sup> software.

## 3. Results

The ultra-high sensitivity of QUIJOTE allowed us to detect the  $J = 4 - 3$  and  $J = 5 - 4$  lines of  $\text{D}^{13}\text{CCCN}$ ,  $\text{DC}^{13}\text{CCN}$ ,  $\text{DCC}^{13}\text{CN}$ ,  $\text{DCCC}^{15}\text{N}$ ,  $\text{H}^{13}\text{C}^{13}\text{CCN}$ ,  $\text{H}^{13}\text{CC}^{13}\text{CN}$ ,  $\text{HC}^{13}\text{C}^{13}\text{CN}$ ,  $\text{HCC}^{13}\text{C}^{15}\text{N}$ , and  $\text{HC}^{13}\text{CC}^{15}\text{N}$  in the 7 mm window. In addition, we identified the  $J = 6 - 5$  line of  $\text{D}^{13}\text{CCCN}$  and  $\text{DCCC}^{15}\text{N}$  at 49.286 GHz and 49.204 GHz, respectively. This complete sample of doubly substituted isotopologues of HCCCN is identified here for the first time in space.

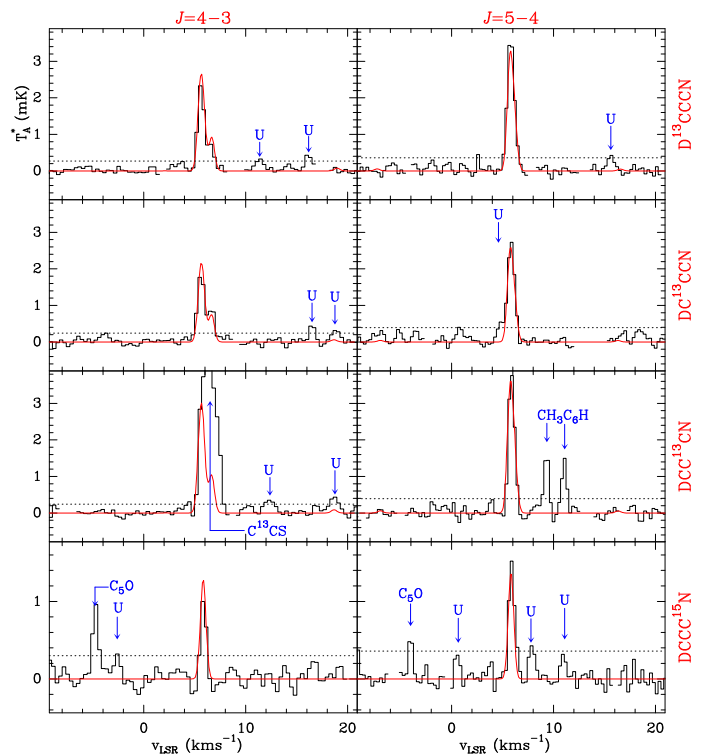


**Fig. 1.** Observed lines of  $\text{D}^{13}\text{CCCN}$ ,  $\text{DC}^{13}\text{CCN}$ ,  $\text{DCC}^{13}\text{CN}$ , and  $\text{DCCC}^{15}\text{N}$  towards TMC-1 (CP) with the Yebes 40 m telescope (histogram black spectra). The red curves present the synthetic spectra obtained using LVG approximation (see Sect. 3.1 and Table A.5). The dashed line represents the  $3\sigma$  level.

The observed lines are shown in Figs. 1 and 2 and are listed in Table A.2. Line identification was performed using the catalogue provided by MADEX (Cernicharo 2012; see Table A.2). An extensive set of laboratory data is available for all these species, except for  $\text{H}^{13}\text{CCC}^{15}\text{N}$  and  $\text{HC}^{13}\text{CC}^{15}\text{N}$ . The laboratory frequencies are taken from de Zafra (1971); Creswell et al. (1977); Mallinson & de Zafra (1978); Plummer et al. (1988); Chen et al. (1991); Yamada et al. (1995); Mbosei et al. (2000); Thorwirth et al. (2000, 2001); Spahn et al. (2008). We fitted these frequencies with a standard Hamiltonian for linear molecules with hyperfine structure to derive their rotational constants. They were implemented in the MADEX code, providing the frequencies shown in Table A.2. To determine the rest frequencies of  $\text{H}^{13}\text{CCC}^{15}\text{N}$  and  $\text{HC}^{13}\text{CC}^{15}\text{N}$ , we predicted their rotational constants from the substitution structure of HCCCN derived from the rotational constants of all its isotopologues measured in the laboratory. One pair of lines was easily found in perfect harmonic relation 5/4 within a few MHz of the predicted frequencies for  $\text{HC}^{13}\text{CC}^{15}\text{N}$ . However, no such pair of lines could be unambiguously identified for  $\text{H}^{13}\text{CCC}^{15}\text{N}$  because it was blended with other strong features. Adopting for  $\text{HC}^{13}\text{CC}^{15}\text{N}$  a distortion constant interpolated between those of the other isotopologues ( $D = 0.509$  kHz), we derive  $B(\text{HC}^{13}\text{CC}^{15}\text{N}) = 4396.6604(5)$  MHz with a standard deviation of the fit of 1.7 kHz. A single-Gaussian function was fitted to the line profiles to obtain the observed line parameters (see Table A.2). The derived radial velocities ( $v_{\text{LSR}}$ ) and line widths ( $\Delta v$ ; full width at half maximum, FWHM) agree with the mean values obtained by Cernicharo et al. (2020a) from Gaussian fits to the 50 lines of  $\text{HC}_5\text{N}$  and its  $^{13}\text{C}$  and  $^{15}\text{N}$  isotopologues detected in this survey. Lines from all the singly substituted isotopologues of HCCCN and from the parent species are

<sup>2</sup> [http://rt40m.oan.es/rt40m\\_en.php](http://rt40m.oan.es/rt40m_en.php)

<sup>3</sup> Surveying the Area of the Neighbour TMC-1 Cloud through Heterodyne Observations

<sup>4</sup> <http://www.iram.fr/IRAMFR/GILDAS/>

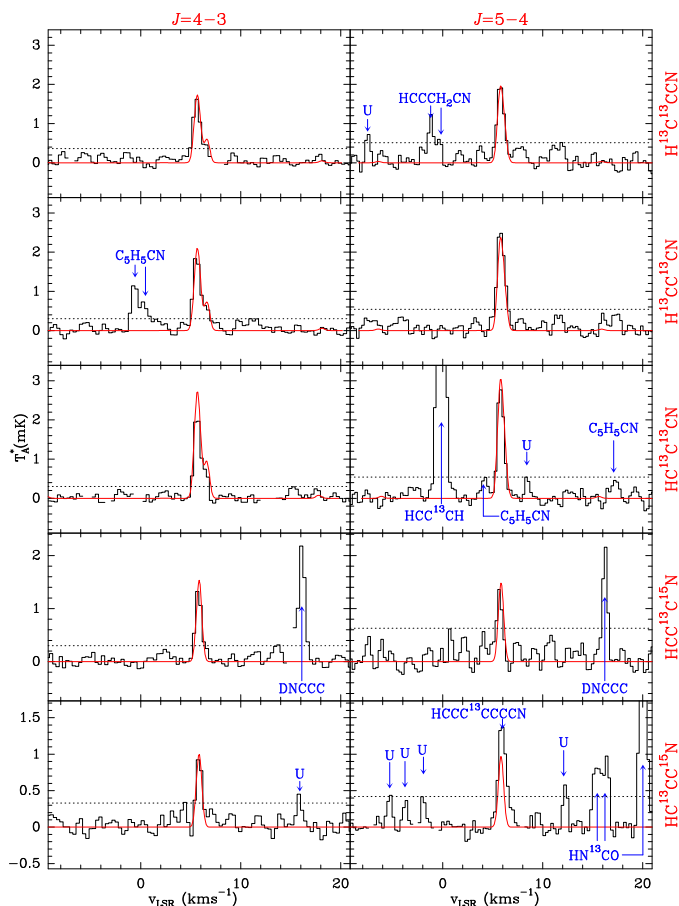


**Fig. 2.** Observed lines of  $\text{H}^{13}\text{C}^{13}\text{CCN}$ ,  $\text{H}^{13}\text{CC}^{13}\text{CN}$ ,  $\text{HC}^{13}\text{C}^{13}\text{CN}$ ,  $\text{HCC}^{13}\text{C}^{15}\text{N}$ , and  $\text{HC}^{13}\text{CC}^{15}\text{N}$  towards TMC-1 (CP) with the Yebes 40 m telescope (histogram black spectra). The red curves show the synthetic spectra obtained using LVG approximation (see Sect. 3.1 and Table A.5). The dashed line represents the  $3\sigma$  level.

identified in the two spectral windows, at 7 mm and 3 mm. Figures A.1, A.2, and A.3 show these detections. The observed line parameters derived from Gaussian fits are listed in Tables A.3 and A.4.

### 3.1. LVG analysis

To derive molecular column densities and constrain the  $\text{H}_2$  volume density in the source, we performed a combined LVG analysis of HCCCN and its isotopologues at 7 mm and 3 mm. For all the studied species, we used the collisional cross sections between HCCCN and para- $\text{H}_2$  provided by Faure et al. (2016). We assumed that the main collider is  $p\text{-H}_2$ , as expected in cold dark clouds (see e.g. Flower et al. 2006).

Firstly, we used the weak hyperfine satellite lines ( $S_r$ ,  $S_w$ , and  $S_b$ ) of the  $J = 4 - 3$  and  $J = 5 - 4$  transitions of HCCCN and the  $J = 4 - 3$  and  $J = 5 - 4$  lines of the singly substituted species (see Fig. A.1) to estimate initial column densities. We assumed a source diameter of  $80''$  (Fossé et al. 2001), a radial velocity of  $5.83 \text{ km s}^{-1}$ , an FWHM of  $0.6 \text{ km s}^{-1}$ , and an excitation temperature of 10 K in agreement with the excitation temperatures derived for the HCCCN isomers (see Cernicharo et al. 2020a) and the kinetic temperature of the source, which was derived using  $\text{NH}_3$  and other symmetric top molecules (see e.g.

<sup>5</sup>  $S_r$ :  $F_u - F_l = J - J$ ;  $S_w$ :  $F_u - F_l = (J - 1) - J$ ;  $S_b$ :  $F_u - F_l = (J - 1) - (J - 1)$ .

Fehér et al. 2016; Agúndez et al. 2023). It is worth noting that these lines are not too sensitive to the excitation temperature as soon as it is higher than 6 – 7 K.

Using these priors, we fitted the density that reproduces the 3 mm lines of the singly substituted isotopologues (Fig. A.3) obtaining a result of  $n(\text{H}_2) = 1 \times 10^4 \text{ cm}^{-3}$ . This value was also derived by Agúndez et al. (2023) using the singly substituted  $^{13}\text{C}$  isotopologues of  $\text{HC}_3\text{N}$ . Using this volume density, we fitted all the lines of the singly substituted isotopologues at 7 mm and 3 mm with a single column density for each species (Figs. A.1 and A.3). To obtain a reasonable fit for the HCCCN lines at 3 mm, we increased the hydrogen volume density to  $n(\text{H}_2) = 2 \times 10^4 \text{ cm}^{-3}$  (Fig. A.2). However, this change in the density arises because the HCCCN lines are optically thick. Consequently, we derived the column density of the doubly substituted isotopologues, detected only at 7 mm, assuming the LVG formalism as well,  $n(\text{H}_2) = 1 \times 10^4 \text{ cm}^{-3}$ ,  $T_K = 10 \text{ K}$ , and the line parameters given above.

The final synthetic spectra obtained from these models reproduce the observed line profiles rather well. Comparisons between model and observation are shown in Figs. 1, 2, A.1, A.2, and A.3. The derived column density values for each species are listed in Table A.5. Owing to the good fits that modelled a large number of observed lines at different frequency domains, and the high signal-to-noise ratio of the observed lines, we assigned as uncertainty to the column density the statistical error derived from error propagation of the root square error of the data.

To evaluate the rotational temperature ( $T_{\text{rot}}$ ), and thus the level of departure from local thermodynamic equilibrium (LTE), and for an independent estimate of the column density ( $N$ ), we also constructed rotation diagrams (see e.g. Goldsmith & Langer 1999) for all species detected at both 3 mm and 7 mm (HCCCN, DCCCN,  $\text{H}^{13}\text{CCCN}$ ,  $\text{HC}^{13}\text{CCN}$ ,  $\text{HCC}^{13}\text{CN}$ , and  $\text{HCCC}^{15}\text{N}$ ) for which a large number of lines are detected (see Appendix B and Table A.5).

### 3.2. Isotopic ratios

From the LVG column densities reported above, we derived the isotopic abundance ratios provided in Table A.5.

A significant number of deuterated molecules has already been detected in the TMC-1 environment (Cabezas et al. 2021a,b, 2022b; Navarro-Almáida et al. 2021). The deuteration fraction is indeed enhanced by several orders of magnitude in cold clouds compared to the elemental D/H ratio of  $\sim 1.5 \times 10^{-5}$  (Linsky 2003) as a result of the significant exothermicity of the reaction  $\text{H}_3^+ + \text{HD} \rightleftharpoons \text{H}_2\text{D}^+ + \text{H}_2$  (192 K), as first pointed out by Watson (1976).

Isotopic exchange reactions may take place for  $^{13}\text{C}$ ,  $^{18}\text{O}$ , and  $^{15}\text{N}$  containing species as well, as suggested first by Langer et al. (1984) and Terzieva & Herbst (2000) and updated later in complex chemical models (Rodgers & Charnley 2008; Roueff et al. 2015; Wirström & Charnley 2018; Loison et al. 2019, 2020; Sipilä et al. 2023). However, the zero-point energy variation is much smaller for the heavier atoms  $^{13}\text{C}$  and  $^{15}\text{N}$ , which induces much lower isotopic enhancements.

For deuterated molecules, we detected both  $\text{DC}_3\text{N}$  and the different D containing isotopologues with one  $^{13}\text{C}$  atom and one  $^{15}\text{N}$  isotopic substitution. The D/H ratios of these different isotopologues are very similar, between 0.013 and 0.018, in agreement with the ratio found by Turner (2001) and Cernicharo et al. (2020a) for DCCCN/HCCCN in the source. HCCCN and DC-CCN are mainly formed via the  $\text{C}_2\text{H}_2 + \text{CN}$ ,  $\text{C}_4\text{H} + \text{N}$  and  $\text{C}_2\text{HD} + \text{CN}$ ,  $\text{C}_4\text{D} + \text{N}$  reactions, respectively, and from the disso-

ciative recombination of  $\text{HC}_3\text{NH}^+$  and  $\text{DC}_3\text{NH}^+$ . The molecular ion  $\text{DC}_3\text{NH}^+$  is enriched in deuterium via the  $\text{HCCCN} + \text{H}_2\text{D}^+$  reaction. The  $\text{DCCCN}/\text{HCCCN}$  ratio is then slightly higher than that of  $\text{C}_4\text{D}/\text{C}_4\text{H}$ , which was found to be 0.008 (Cabezas et al. 2021b). Similar reactions are most probably involved in the  $^{13}\text{C}$  substituted species.

We detect singly and doubly  $^{13}\text{C}$  substituted  $\text{HCCCN}$  as well as  $^{13}\text{C}$  plus  $^{15}\text{N}$  substitutions with different locations of  $^{13}\text{C}$ . The  $\text{C}/^{13}\text{C}$  ratios derived from the different isotopologue substitutions of  $\text{HCCCN}$  show a clear fractionation for the species with the  $^{13}\text{C}$  isotope adjacent to the nitrogen atom that corresponds to the most stable system as shown in Takano et al. (1998). Under thermodynamic equilibrium,  $\text{HCC}^{13}\text{CN}$  is predicted to be more abundant by a factor of 2 than  $\text{HC}^{13}\text{CCN}$  at 10 K (Wolfsberg et al. 1979). The same factor of 2 is predicted for the  $\text{HC}^{13}\text{CCN}/\text{H}^{13}\text{CCCN}$  ratio at the same temperature, following the respective zero-point energy values. However, this feature is not seen in the observations. Kinetic effects rather than thermodynamic considerations are indeed at work under interstellar conditions.

Most of the derived  $\text{C}/^{13}\text{C}$  abundance ratios are  $\sim 95$  and  $\sim 105$ , consistent with but slightly higher than the Solar System value of 89 (Wilson & Rood 1994). The standard value of  $\sim 70$  in the local ISM (see e.g. Wilson & Rood 1994; Ritchey et al. 2011) is similar to the values between 55 and 80 that we found for the enhanced species, that is, the carbon near nitrogen. The  $\text{C}/^{13}\text{C}$  ratio in deuterated cyanoacetylene is close to 100, with a slightly lower value for the most stable  $\text{DCC}^{13}\text{CN}$  isotopologue and rising up to 132 for  $\text{DC}^{13}\text{CCN}$ . This could indicate a light dilution of the  $\text{DC}^{13}\text{CCN}$  abundances with respect to the other  $^{13}\text{C}$  isotopologues of  $\text{DCCCN}$ . The relative abundance ratios are 1.0:1.1:1.6 for  $\text{H}^{13}\text{CCCN}:\text{HC}^{13}\text{CCN}:\text{HCC}^{13}\text{CN}$ , similar to the ratios reported previously in TMC-1 (Takano et al. 1998), L1527 (Araki et al. 2016), and L1521B (Taniguchi et al. 2017). On the other hand, the  $^{13}\text{C}$  isotopologues of the deuterated species show relative abundances of 1.3:1.0:1.4 for  $\text{D}^{13}\text{CCCN}:\text{DC}^{13}\text{CCN}:\text{DCC}^{13}\text{CN}$ , which indicate different enhancement routes for  $^{13}\text{C}$  in  $\text{HCCCN}$  and  $\text{DCCCN}$ . We note that the three  $^{13}\text{C}$  isotopologues of  $\text{HCCCN}$  and  $\text{HNCCC}$  are in an abundance ratio close to  $\sim 95$ , and therefore, these  $\text{HCCCN}$  isomers do not present fractionation depending on the position of the  $^{13}\text{C}$  atom (Cernicharo et al. 2024).

It is worth noting that for cold sources, the relative abundance ratios of the  $^{13}\text{C}$  isotopologues of  $\text{HC}_3\text{N}$  is not dependent on the evolutionary state of the source. The abundances in L1527, however, which is in an evolved evolutionary state (protostellar core), are similar to those of the starless cores TMC-1 and L1521B. Other cold cores present different relative abundances: 1.0:1.1:1.2 for L483 (protostellar core; Agúndez et al. 2019) or 1.5:1.0:2.1 for L134N (starless core; Taniguchi et al. 2017). All these sources present kinetic temperatures between 9 and 14 K (Agúndez et al. 2023).

Takano et al. (1998) pointed out that the  $\text{HCC}^{13}\text{CN}$  fractionation is consistent with  $\text{C}_2\text{H}_2 + \text{CN}$  reaction as the main formation route for  $\text{HCCCN}$  when we assume that the triple bond of  $\text{C}_2\text{H}_2$  is conserved without breaking in the reaction (and then the abundances of  $\text{H}^{13}\text{CCCN}$  and  $\text{HC}^{13}\text{CCN}$  remain equal to each other) and the CN molecule introduces the  $^{13}\text{C}$  enriched carbon into  $\text{HCCCN}$ . The observed fractionation also excludes isotope exchange with  $\text{HCCCN}$  as the main process for the formation of the  $^{13}\text{C}$  isotopologues.

For the double isotopologues, we also found an enhancement of  $\text{H}^{13}\text{CC}^{13}\text{CN}$  and  $\text{HC}^{13}\text{C}^{13}\text{CN}$  relative to  $\text{H}^{13}\text{C}^{13}\text{CCN}$  and of  $\text{HCC}^{13}\text{C}^{15}\text{N}$  relative to  $\text{HC}^{13}\text{CC}^{15}\text{N}$ , which points to a fraction-

ation for all the non-deuterated double isotopologues in which the  $^{13}\text{C}$  isotope is adjacent to the nitrogen atom. For these cases, isotope exchange with  $\text{HCC}^{13}\text{CN}$  might proceed as an important route for the formation of these double isotopologues.

For the  $^{15}\text{N}$  substitutions, the isotopic ratios of the hydrogen and deuterated cyano-acetylene are very similar, with respective values of 317 and 330. The values derived for the  $^{13}\text{C}$  containing  $^{15}\text{N}$  isotopes are slightly lower, equal to  $\sim 250$  and independent of the  $^{13}\text{C}$  position. The measured  $\text{N}/^{15}\text{N}$  ratios in the local ISM differ by up to a factor of two (see e.g. Agúndez et al. 2019), with values in the range of 237 – 450. Our derived abundance ratios, between 250 and 330, are consistent with the local ISM values. These results also agree with previous values found in TMC-1 (Taniguchi & Saito 2017) and in other cold cores (Agúndez et al. 2019; Magalhães et al. 2018; Hily-Blant et al. 2018).

## 4. Discussion

The results of Sect. 3.2 show a  $^{13}\text{C}$  fractionation for all the simple and double isotopologues in which  $^{13}\text{C}$  is adjacent to the nitrogen atom, except for  $\text{DCC}^{13}\text{CN}$ , which suggests different enhancement routes for  $^{13}\text{C}_3$  in  $\text{HCCCN}$  and  $\text{DCCCN}$  and may indicate different formation routes for  $\text{HCCCN}$  and  $\text{DCCCN}$ . To further explore this hypothesis, we exploited the SANCHO data to produce maps of the spatial distribution of  $\text{HCCCN}$  and all its singly substituted isotopologues (Fig. A.4). All data within a circle of  $20''$  were averaged spatially with equal weight. At low frequency, this represents a small degradation of the spatial resolution. However, at the highest frequency in the Q band, the effective angular resolution is  $\sim 1.4$  higher than the half-power beam width (HPBW) of the telescope and produces a broadening of the spatial structures. Nevertheless, this results in an effective spatial resolution that is roughly identical in the Q band. A detailed description of the data reduction procedure was presented in Cernicharo et al. (2023b). The  $\text{HCCCN}$  map was obtained using the integrated intensity of the weak satellite hyperfine lines ( $S_r$ ,  $S_w$ , and  $S_b$ ). This guarantees low line opacities, and therefore, the integrated intensities are proportional to the column densities. The maps of  $\text{DCCCN}$ ,  $\text{H}^{13}\text{CCCN}$ ,  $\text{HC}^{13}\text{CCN}$ , and  $\text{HCC}^{13}\text{CN}$  correspond to the sum of the integrated intensity of all hyperfine lines for each transition.

As shown in Fig. A.4, the integrated emission of all the isotopologues follows the well-known filamentary structure of TMC-1 with a dense condensation around the central position. The SANCHO maps show that the emission peak of the integrated intensity of  $\text{HCCCN}$  and other cyanopolynes (see also Cernicharo et al. 2023b) is displaced with respect to the coordinates of our QUIJOTE survey, which is widely assumed as the CP of TMC-1 (see e.g. Kaifu et al. 2004; McGuire et al. 2020). However, whereas the intensity peak is located at a south-east position from the centre of the map (the CP peak) for  $\text{HCCCN}$ ,  $\text{H}^{13}\text{CCCN}$ ,  $\text{HC}^{13}\text{CCN}$ ,  $\text{HCC}^{13}\text{CN}$ , and  $\text{HCCC}^{15}\text{N}$ , the deuterated isotopologue emission peaks at a significantly different position, north-east of the CP peak. These two peaks are displaced by about  $\sim 40''$ . Figure A.4 therefore shows that  $\text{DCCCN}$  alone does not present a clear co-emission with the main isotopologue. This finding also points to different formations routes for the deuterated and non-deuterated isotopologues of  $\text{HCCCN}$ . In addition, because deuterium fractionation is more efficient at low temperatures, we could also expect that  $\text{DCCCN}$  traces a colder or denser region of the cloud. In this context, we note that the  $\text{DCCCN}$  map resembles the two  $\text{HC}_7\text{N}$  maps presented in Cernicharo et al. (2023b), which were performed with lines of high-energy transitions ( $J = 28 - 27$  at  $E_{\text{upp}} = 22.0$  K and  $J = 38 - 37$

at  $E_{\text{upp}} = 40.1$  K). Although the high signal-to-noise ratio of the HC<sub>7</sub>N lines provides good-quality maps, these high-energy transitions are very sensitive to the density or to small changes in the kinetic temperature. We therefore cannot compare this directly with the low-energy DCCCN emission. This prevents us from drawing stronger conclusions about the temperature or density structure of the source.

## 5. Conclusions

The QUIJOTE survey of TMC-1 allowed us to identify a complete and coherent sample of doubly substituted isotopologues of HCCCN in space for the first time. We detected D<sup>13</sup>CCCN, DC<sup>13</sup>CCN, DCC<sup>13</sup>CN, DCCC<sup>15</sup>N, H<sup>13</sup>C<sup>13</sup>CCN, H<sup>13</sup>CC<sup>13</sup>CN, HC<sup>13</sup>C<sup>13</sup>CN, HCC<sup>13</sup>C<sup>15</sup>N, and HC<sup>13</sup>CC<sup>15</sup>N through their  $J = 4 - 3$  and  $J = 5 - 4$  lines in the 7 mm window. We derived column densities for all the singly and doubly substituted isotopologues and physical properties of the source using LVG approximation. For HCCCN and its singly substituted isotopologues, we found consistent values in the two observed spectral bands, 7 mm and 3 mm, and with  $n(\text{H}_2) = 1 \times 10^4 \text{ cm}^{-3}$  and  $T = 10$  K. The column density ratios between different isotopologues show a slight <sup>13</sup>C fractionation for HCC<sup>13</sup>CN and other doubly substituted isotopologues in which a <sup>13</sup>C atom lies adjacent to the nitrogen atom. This is not the case for DCC<sup>13</sup>CN, which points to additional chemical discrimination for deuterated isotopologues of HCCCN. This hypothesis is supported by the SANCHO data, which allow the comparison of the spatial distribution of HCCCN and that of its singly substituted isotopologues. The emission peak of the spatial distribution of the deuterated species appears to be displaced by  $\sim 40''$  with respect to that of the remaining singly substituted isotopologues, suggesting different enhancement routes for the different isotopologues of HCCCN.

*Acknowledgements.* We thank the anonymous referee for helpful comments and suggestions that improved the presentation of this paper significantly. We acknowledge funding support from the European Research Council (ERC Synergy Grant 610256: NANOCOSMOS). We also thank the Spanish MICIN for funding support under grants PID2019-106110GB-I00, PID2019-107115GB-C21, and PID2019-106235GB-I00. This research has been also funded by grant PID2022-137980NB-I00 by the Spanish Ministry of Science and Innovation/State Agency of Research MCIN/AEI/10.13039/501100011033 and by “ERDF A way of making Europe”.

## References

Agúndez, M., Cabezas, C., Tercero, B., et al. 2021, *A&A*, 647, L10  
 Agúndez, M., Marcelino, N., Cernicharo, J., Roueff, E., & Tafalla, M. 2019, *A&A*, 625, A147  
 Agúndez, M., Marcelino, N., Tercero, B., Jiménez-Serra, I., & Cernicharo, J. 2023, *A&A*, 677, A106  
 Araki, M., Takano, S., Sakai, N., et al. 2016, *ApJ*, 833, 291  
 Belloche, A., Müller, H. S. P., Garrod, R. T., & Menten, K. M. 2016, *A&A*, 587, A91  
 Cabezas, C., Agúndez, M., Marcelino, N., et al. 2022a, *A&A*, 657, L4  
 Cabezas, C., Endo, Y., Roueff, E., et al. 2021a, *A&A*, 646, L1  
 Cabezas, C., Fuentetaja, R., Roueff, E., et al. 2022b, *A&A*, 657, L5  
 Cabezas, C., Roueff, E., Tercero, B., et al. 2021b, *A&A*, 650, L15  
 Cernicharo, J. 1985, Internal IRAM Report (Granada: IRAM)  
 Cernicharo, J. 2012, in *EAS Publications Series*, Vol. 58, EAS Publications Series, ed. C. Stehlé, C. Joblin, & L. d’Hendecourt, 251–261  
 Cernicharo, J., Agúndez, M., Cabezas, C., et al. 2021a, *A&A*, 649, L15  
 Cernicharo, J., Agúndez, M., Kaiser, R. I., et al. 2021b, *A&A*, 652, L9  
 Cernicharo, J., Cabezas, C., Agúndez, M., et al. 2021c, *A&A*, 648, L3  
 Cernicharo, J., Fuentetaja, R., Agúndez, M., et al. 2023a, *A&A*, 680, L4  
 Cernicharo, J., Marcelino, N., Agúndez, M., et al. 2020a, *A&A*, 642, L8  
 Cernicharo, J., Marcelino, N., Pardo, J. R., et al. 2020b, *A&A*, 641, L9  
 Cernicharo, J., Marcelino, N., Roueff, E., et al. 2012, *ApJ*, 759, L43  
 Cernicharo, J., Tercero, B., Cabezas, C., et al. 2024, Accepted *A&A*

Cernicharo, J., Tercero, B., Marcelino, N., Agúndez, M., & de Vicente, P. 2023b, *A&A*, 674, L4  
 Chen, W., Bocquet, R., Włodarczyk, G., & Boucher, D. 1991, *International Journal of Infrared and Millimeter Waves*, 12, 987  
 Creswell, R. A., Winnewisser, G., & Gerry, M. C. L. 1977, *Journal of Molecular Spectroscopy*, 65, 420  
 de Zafra, R. L. 1971, *ApJ*, 170, 165  
 Faure, A., Lique, F., & Wiesenfeld, L. 2016, *MNRAS*, 460, 2103  
 Fehér, O., Tóth, L. V., Ward-Thompson, D., et al. 2016, *A&A*, 590, A75  
 Flower, D. R., Pineau Des Forêts, G., & Walmsley, C. M. 2006, *A&A*, 449, 621  
 Fossé, D., Cernicharo, J., Gerin, M., & Cox, P. 2001, *ApJ*, 552, 168  
 Goldsmith, P. F. & Langer, W. D. 1999, *ApJ*, 517, 209  
 Hily-Blant, P., Faure, A., Vastel, C., et al. 2018, *MNRAS*, 480, 1174  
 Kaifu, N., Ohishi, M., Kawaguchi, K., et al. 2004, *PASJ*, 56, 69  
 Langer, W. D., Graedel, T. E., Frerking, M. A., & Armentrout, P. B. 1984, *ApJ*, 277, 581  
 Linsky, J. L. 2003, *Space Sci. Rev.*, 106, 49  
 Loison, J.-C., Wakelam, V., Gratier, P., & Hickson, K. M. 2019, *MNRAS*, 484, 2747  
 Loison, J.-C., Wakelam, V., Gratier, P., & Hickson, K. M. 2020, *MNRAS*, 498, 4663  
 Magalhães, V. S., Hily-Blant, P., Faure, A., Hernandez-Vera, M., & Lique, F. 2018, *A&A*, 615, A52  
 Mallinson, P. D. & de Zafra, R. L. 1978, *Molecular Physics*, 36, 827  
 Marcelino, N., Agúndez, M., Tercero, B., et al. 2020, *A&A*, 643, L6  
 Marcelino, N., Puzzarini, C., Agúndez, M., et al. 2023, *A&A*, 674, L13  
 Mbosei, L., Fayt, A., Dréan, P., & Cosléou, J. 2000, *Journal of Molecular Structure*, 517-518, 271  
 McGuire, B. A., Burkhardt, A. M., Loomis, R. A., et al. 2020, *ApJ*, 900, L10  
 Navarro-Almada, D., Fuente, A., Majumdar, L., et al. 2021, *A&A*, 653, A15  
 Pardo, J. R., Cernicharo, J., & Serabyn, E. 2001, *IEEE Transactions on Antennas and Propagation*, 49, 1683  
 Plummer, G. M., Mauer, D., Yamada, K. M. T., & Möller, K. 1988, *Journal of Molecular Spectroscopy*, 130, 407  
 Ritchey, A. M., Federman, S. R., & Lambert, D. L. 2011, *ApJ*, 728, 36  
 Rodgers, S. D. & Charnley, S. B. 2008, *ApJ*, 689, 1448  
 Roueff, E., Loison, J. C., & Hickson, K. M. 2015, *A&A*, 576, A99  
 Schmidt, D. R. & Ziurys, L. M. 2019, *ApJ*, 881, L38  
 Sipilä, O., Colzi, L., Roueff, E., et al. 2023, *A&A*, 678, A120  
 Spahn, H., Müller, H. S. P., Giesen, T. F., et al. 2008, *Chemical Physics*, 346, 132  
 Takano, S., Masuda, A., Hirahara, Y., et al. 1998, *A&A*, 329, 1156  
 Taniguchi, K., Ozeki, H., & Saito, M. 2017, *ApJ*, 846, 46  
 Taniguchi, K. & Saito, M. 2017, *PASJ*, 69, L7  
 Tercero, F., López-Pérez, J. A., Gallego, J. D., et al. 2021, *A&A*, 645, A37  
 Terzieva, R. & Herbst, E. 2000, *MNRAS*, 317, 563  
 Thorwirth, S., Mueller, H. S. P., & Winnewisser, G. 2001, *Physical Chemistry Chemical Physics (Incorporating Faraday Transactions)*, 3, 1236  
 Thorwirth, S., Müller, H. S. P., & Winnewisser, G. 2000, *Journal of Molecular Spectroscopy*, 204, 133  
 Turner, B. E. 2001, *ApJS*, 136, 579  
 Watson, W. D. 1976, *Reviews of Modern Physics*, 48, 513  
 Wilson, T. L. & Rood, R. 1994, *ARA&A*, 32, 191  
 Wirstrom, E. S. & Charnley, S. B. 2018, *MNRAS*, 474, 3720  
 Wolfsberg, M., Bopp, P., Heinzinger, K., & Mallinson, P. D. 1979, *A&A*, 74, 369  
 Yamada, K. M. T., Moravec, A., & Winnewisser, G. 1995, *Zeitschrift Naturforschung Teil A*, 50, 1179

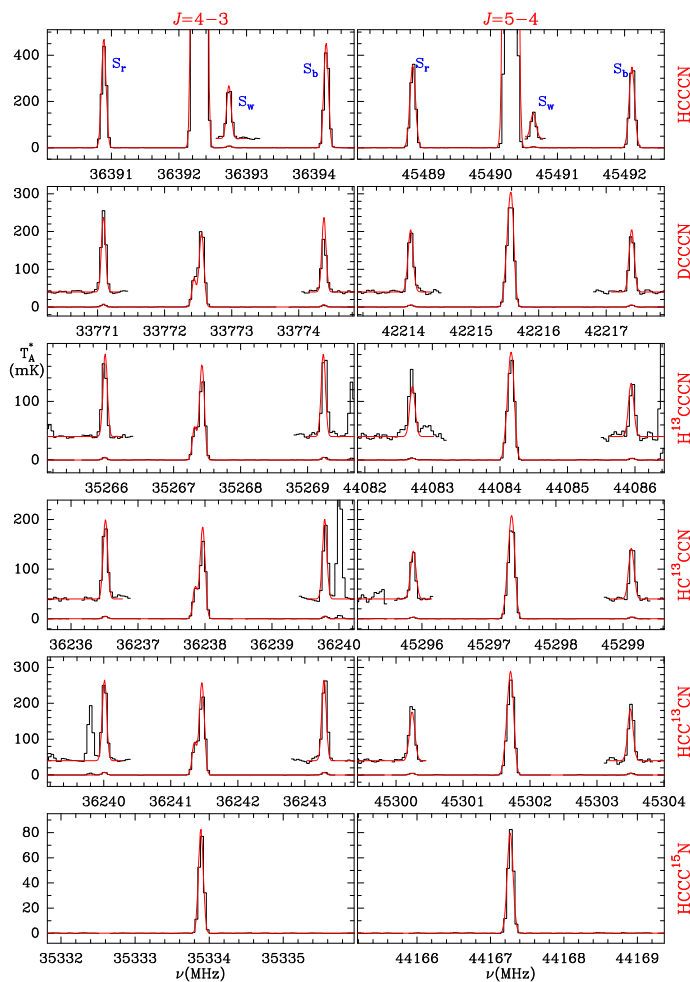


**Fig. A.1.** Observed lines of HCCCN, DCCCN, H<sup>13</sup>CCCN, HC<sup>13</sup>CCN, HCC<sup>13</sup>CN, and HCCC<sup>15</sup>N towards TMC-1 (CP) at 7 mm (histogram black spectra). The red curves show the synthetic spectra obtained using the LVG approximation (see Sect. 3.1 and Table A.5). The weak satellite hyperfine lines ( $S_w$  for HCCCN and  $S_r$  and  $S_b$  for the isotopologues) have been offsetted and multiplied by a factor of 30. These hyperfine lines correspond to the transitions  $F_u - F_l = J - J$  for  $S_r$ ,  $F_u - F_l = (J - 1) - J$  for  $S_w$ , and  $F_u - F_l = (J - 1) - (J - 1)$  for  $S_b$ .

## Appendix A: Additional figures and tables

Additional figures and tables are shown in this appendix. Table A.1 shows details of the efficiencies and HPBW for the Yebes 40 m and the IRAM 30 m telescopes (see Sect. 2). Observational and spectroscopic line parameters for the detected lines (see Sect. 3) and the excitation temperature derived for each transition using the LVG formalism (see Appendix B) are shown in Tables A.2, A.3, and A.4. Table A.5 shows the derived column density values for each species using the LVG approximation (see Sect. 3.1) and the rotational diagram procedure (see Appendix B), and the derived isotopic abundance ratios (see Sect. 3.2).

The detected lines from all the singly substituted isotopologues of HCCCN and from the parent species (see Sect. 3) and the synthetic spectra derived using the LVG approximation (see Sect. 3.1) are shown in Figs. A.1, A.2, and A.3. Figure A.4 shows the spatial distribution of the integrated intensity between 5.3 km s<sup>-1</sup> and 6.5 km s<sup>-1</sup> of the  $J = 4 - 3$  and  $J = 5 - 4$  lines of HCCCN and its singly substituted isotopologues detected in the SANCHO survey.

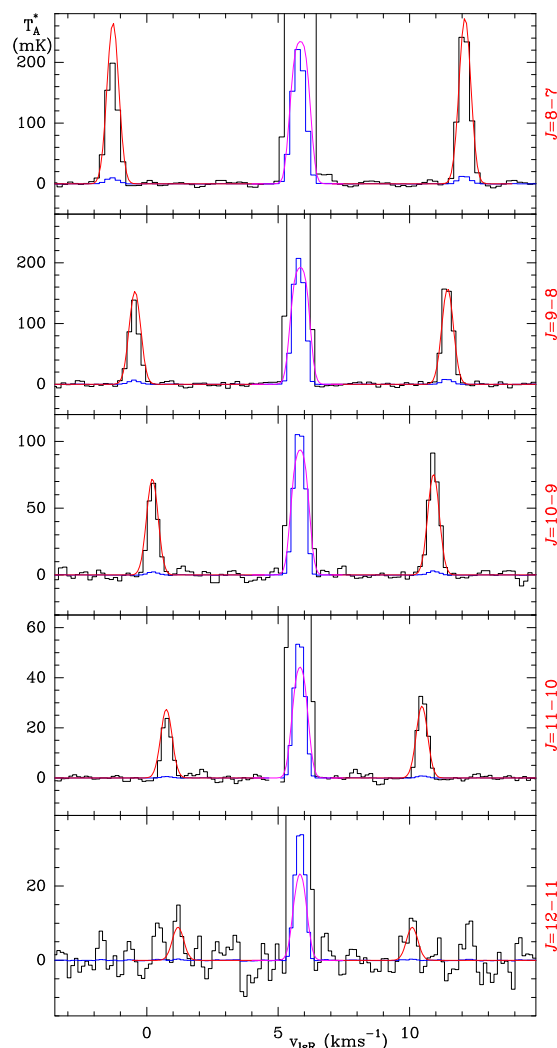


**Fig. A.2.** Observed lines of HCCCN towards TMC-1 (CP) at 3 mm (histogram black spectra). The blue histogram spectra show the data divided by a factor of 20, 20, 30, 40, and 40, from top to bottom. The red curves show the synthetic spectra obtained using the LVG approximation (see Sect. 3.1 and Table A.5). The magenta curves show the synthetic spectra divided by the same factors as above.

## Appendix B: Rotational diagrams

To evaluate the rotational temperature ( $T_{rot}$ ), and thus, the level of departure from LTE, and to obtain an independent estimate of the column density ( $N$ ), we constructed rotation diagrams (see e.g. Goldsmith & Langer 1999) for all species detected at both 3 mm and 7 mm (HCCCN, DCCCN, H<sup>13</sup>CCCN, HC<sup>13</sup>CCN, HCC<sup>13</sup>CN, and HCCC<sup>15</sup>N) for which a large number of lines are detected. For the double isotopologues, only two lines are detected, so that the rotational diagram method does not provide a reliable determination of the column density and the rotational temperature.

This analysis assumes the Rayleigh-Jeans approximation, optically thin lines, and local thermodynamic equilibrium conditions. The equation that derives the total column density under these conditions can be re-arranged as

$$\ln \left( \frac{8\pi k_B v^2 \int T_{MB} dv}{hc^3 A_{ul} g_u b} \right) = \ln \left( \frac{N}{Q_{rot}} \frac{T_{rot} - T_{bg}}{T_{rot}} \right) - \frac{E_u}{k_B T_{rot}}, \quad (\text{B.1})$$

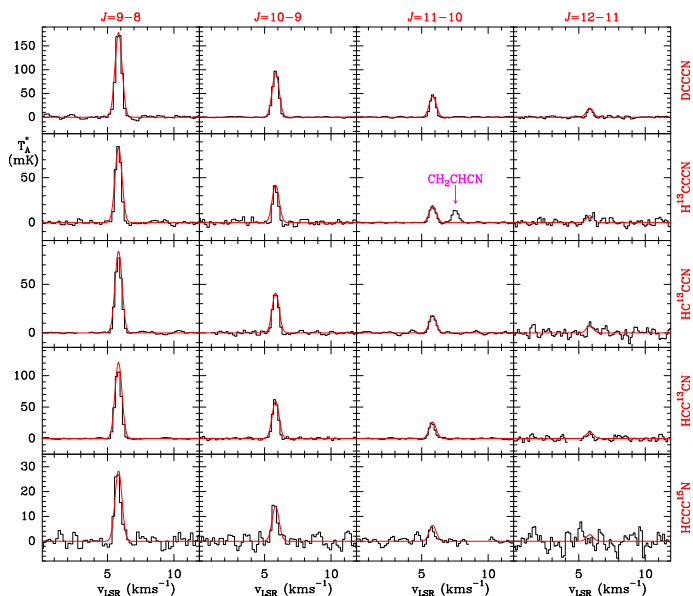


**Fig. A.3.** Observed lines of DCCCN,  $\text{H}^{13}\text{CCCN}$ ,  $\text{HC}^{13}\text{CCN}$ ,  $\text{HCC}^{13}\text{CN}$ , and  $\text{HCCC}^{15}\text{N}$  towards TMC-1 (CP) at 3 mm (histogram black spectra). The red curves show the synthetic spectra obtained using the LVG approximation (see Sect. 3.1 and Table A.5).

**Table A.1.** Half-power beam width, main-beam efficiency, and forward efficiency of the Yebes 40 m and IRAM 30 m radiotelescopes in the Q and W bands, respectively.

Frequency (GHz)	Wavelength (mm)	HPBW ( $''$ )	$\eta_{\text{MB}}$	$\eta_{\text{F}}$
Q band <sup>a</sup>				
32.4	9.2	54.4	0.66	0.95
34.6	8.6	50.9	0.62	0.95
36.9	8.1	47.8	0.60	0.95
39.2	7.6	45.0	0.59	0.95
41.5	7.2	42.5	0.58	0.95
43.8	6.8	40.2	0.56	0.95
46.1	6.5	38.2	0.54	0.95
48.4	6.2	36.4	0.51	0.93
W band <sup>b</sup>				
72.0	4.2	34.2	0.83	0.95
86.0	3.5	28.6	0.81	0.95
100.0	3.0	24.0	0.80	0.95
115.0	2.6	21.4	0.78	0.94

**Notes.** <sup>(a)</sup> QUIJOTE and SANCHO data recorded with the Yebes 40 m telescope (see Sect. 2). [https://rt40m.oan.es/rt40m\\_en.php](https://rt40m.oan.es/rt40m_en.php). <sup>(b)</sup> The 3 mm survey of TMC-1 recorded with the IRAM 30 m telescope (see Sect. 2). <https://publicwiki.iram.es/Iram30mEfficiencies>.

where  $g_u$  is the statistical weight in the upper level,  $A_{ul}$  is the Einstein A-coefficient for spontaneous emission,  $Q_{\text{rot}}$  is the rotational partition function (which depends on  $T_{\text{rot}}$ ),  $E_u$  is the upper level energy,  $\nu$  is the frequency of the transition,  $b$  is the dilution factor, and  $T_{\text{bg}}$  is the cosmic microwave background radiation temperature. The first term of Eq. (B.1), which only depends on spectroscopic and observational line parameters, is plotted as a function of  $E_u/k_{\text{B}}$  for the different detected lines. Thus,  $T_{\text{rot}}$  and

$N$  can be derived by performing a linear least-squares fit to the points (see Fig. B.1).

For HCCCN, DCCCN,  $\text{H}^{13}\text{CCCN}$ ,  $\text{HC}^{13}\text{CCN}$ , and  $\text{HCC}^{13}\text{CN}$  different hyperfine structure components of the same  $J_u - J_l$  transition are observed or are blended in a single line, depending on the frequency of the transition. Thus, to correctly determine  $T_{\text{rot}}$  and  $N$ , the integrated intensity ( $\int T_{\text{MB}} dv$ ), the level degeneracy ( $g$ ), and the line strength ( $S$ ) were calculated as the sum of all hyperfine components of each  $J_u - J_l$  transition. The characteristic frequency ( $\nu$ ) was determined using the weighted average with the relative strength of each hyperfine line as weight, and the Einstein coefficient ( $A$ ) was calculated using the usual relation. Due to opacity effects for the different hyperfine components of HCCCN, to derive a reliable column density for this species, the observed integrated intensity for each  $J_u - J_l$  transition was assumed as the integrated intensity of the  $S_r$  satellite line multiplied by a factor of the inverse of the relative intensity (according to the different line strengths) of this hyperfine line with respect to the remaining components of the same  $J_u - J_l$  transition.

The results for  $T_{\text{rot}}$  and  $N$  using the population diagram procedure are shown in Table A.5 and Fig. B.1. The uncertainties were calculated using the statistical errors given by the linear least-squares fit for the slope and the intercept. The individual errors of the data points are those derived by least squares, taking into account the uncertainty obtained in the determination of the observed integrated intensity (see Tables A.2, A.3, and A.4).

We obtained rotational temperatures between 4.1 K and 5.0 K for HCCCN and its single isotopologues (see Fig. B.1), indicating that they are subthermally excited, like most of the species with three to five atoms in this region and in cold dark clouds (see e.g. Cernicharo et al. 2020a,b; Marcelino et al. 2020; Agúndez et al. 2023), and consistent with the derived  $\text{H}_2$  density. We find higher excitation temperatures, closer to the kinetic temperature of 10 K, for the  $J = 4 - 3$  and  $J = 5 - 4$  lines using the LVG formalism (see Tables A.2, A.3, and A.4). However, for the lines at 3 mm, the derived excitation temperatures are about 4-5 K. As the excitation temperature derived from the rotational diagrams is determined by the slope, which is dominated by the 3 mm lines, we found these large differences between the excitation temperatures derived with the rotational diagrams and the kinetic temperature assumed for the LVG modelling. Moreover, in these diagrams, the correction for the background temperature introduces a non-linear dependence that might introduce some uncertainty in the determination of the rotational temperatures, especially for low-excitation temperatures. On the other hand, the column densities derived using this method are dominated by the contribution of the low-energy  $J = 4 - 3$  and  $J = 5 - 4$  lines at 7 mm. The column densities derived through the rotation diagram are systematically higher by  $\sim 30 - 50\%$  than those derived through the LVG analysis (see Table A.5). These differences mainly arise because various assumptions made in the frame of the rotation diagram method break down (see Agúndez et al. 2023). We therefore adopted as preferred values for the column densities the values that were derived through the LVG method, which should also provide more accurate values as long as the collision rate coefficients with para- $\text{H}_2$  and the gas kinetic temperature are known accurately.

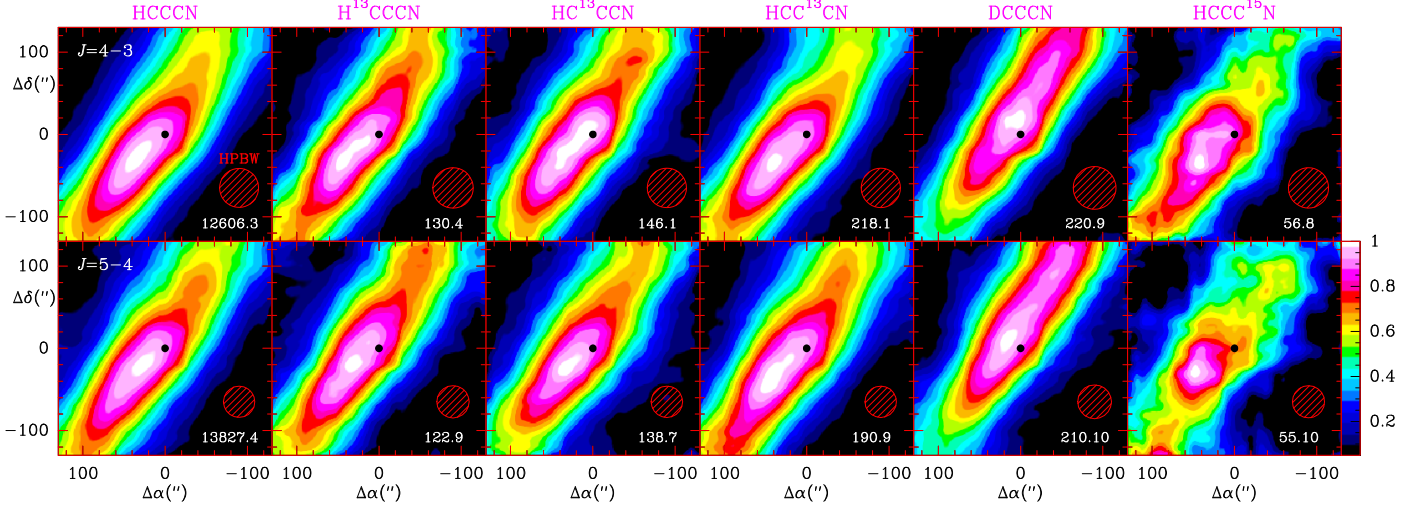


**Fig. A.4.** Colour plot of the spatial distribution of the integrated intensity between  $5.3 \text{ km s}^{-1}$  and  $6.5 \text{ km s}^{-1}$  of the  $J = 4 - 3$  and  $J = 5 - 4$  lines of HCCCN and its singly substituted isotopologues detected in the SANCHOC survey. The sampling of the data is  $20''$ , and the integrating area in each position corresponds to a circle with a radius of  $20''$  (see Sect. 4). For each species, the integrated intensity has been normalized to the maximum value within the area covered by the map. The colour scale is therefore the same for all species and is indicated by the wedge in the lower right part of the figure. The maximum intensities (in  $\text{mK km s}^{-1}$ ) are indicated in the bottom right corner of each panel. The HPBW of the telescope is also indicated in the bottom right corner of each map. The black dot indicates the centre of the map, which corresponds to the QUIJOTE survey position, i.e. the cyanopolyne peak of TMC-1.

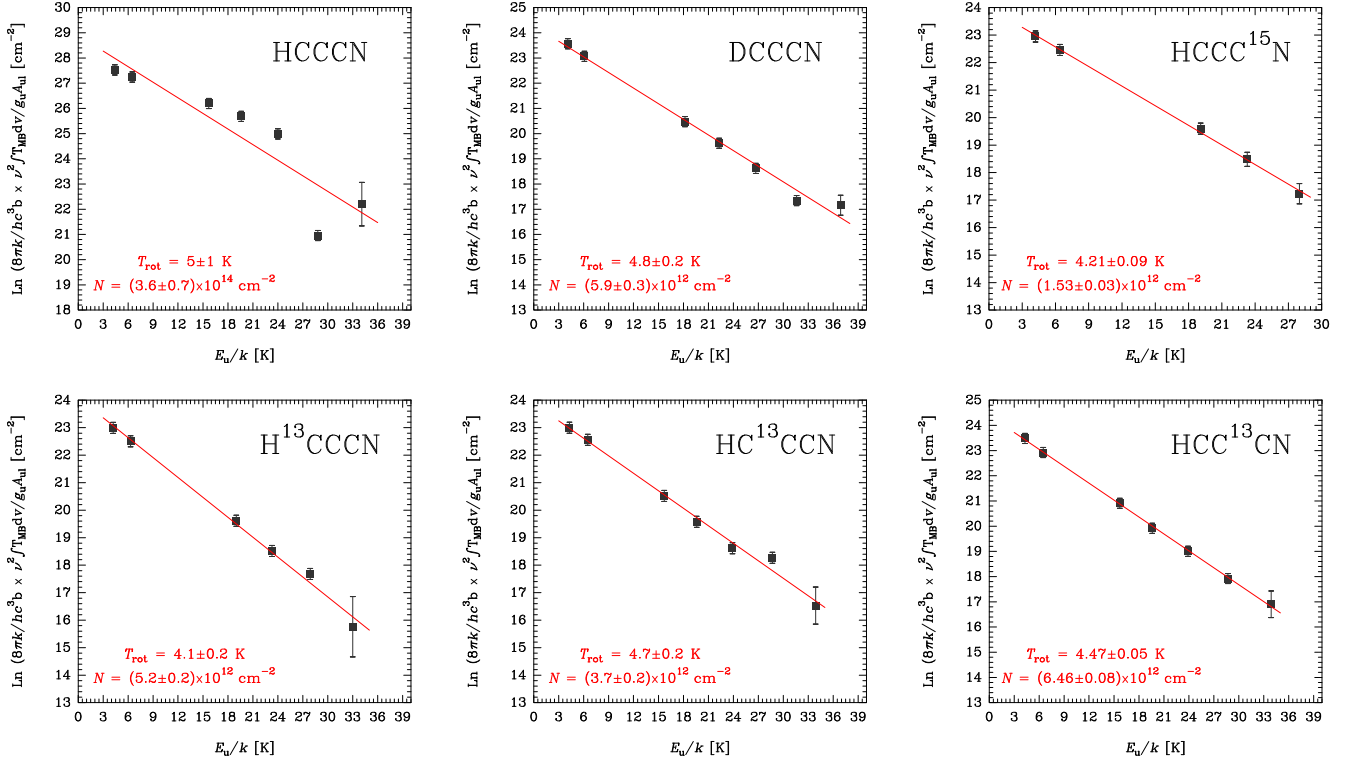


**Fig. B.1.** Rotational diagrams of HCCCN and its singly substituted isotopologues towards TMC-1 (CP). The derived values of the rotational temperature,  $T_{\text{rot}}$ , the column density,  $N$ , and their respective uncertainties are indicated for each species.



**Table A.2.** Spectroscopic and observed line parameters for the doubly substituted isotopologues of HCCCN in TMC-1.

Molecule	$J_u - J_l$	$\nu_{\text{rest}}^a$ (MHz)	$E_u/k_B$ (K)	$S_{ij}$	$T_A^*$ (mK)	$v_{\text{LSR}}^b$ (km s <sup>-1</sup> )	$\Delta v^c$ (km s <sup>-1</sup> )	$\int T_A^* dv^d$ (mK km s <sup>-1</sup> )	$\sigma^e$ (mK)	$T_{\text{ex}}^f$ (K)
D <sup>13</sup> CCCN	4–3 <sup>g</sup>	32857.4694(09)	3.9	2.86	0.70	5.74(07)	0.75(17)	0.56(06)	0.09	7.4
D <sup>13</sup> CCCN	4–3 <sup>h</sup>	32857.5804(09)	3.9	8.64 <sup>i</sup>	2.38	5.77(02)	0.75(05)	1.90(19)	0.09	7.6/8.8
D <sup>13</sup> CCCN	5–4 <sup>j</sup>	41071.8709(10)	5.9	14.6 <sup>i</sup>	3.67	5.78(01)	0.84(03)	3.29(33)	0.12	6.4/6.4/6.2
D <sup>13</sup> CCCN	6–5 <sup>j</sup>	49286.1351(13)	8.3	17.7 <sup>i</sup>	3.08	5.84(02)	0.53(05)	1.75(17)	0.32	5.6/5.6/5.3
DC <sup>13</sup> CCN	4–3 <sup>g</sup>	33660.2341(06)	4.0	2.86	0.94	5.86(04)	0.63(11)	0.63(06)	0.08	7.3
DC <sup>13</sup> CCN	4–3 <sup>h</sup>	33660.3452(06)	4.0	8.64 <sup>i</sup>	1.87	5.78(02)	0.85(05)	1.67(17)	0.08	7.4/8.5
DC <sup>13</sup> CCN	5–4 <sup>jk</sup>	42075.3228(08)	6.1	14.6 <sup>i</sup>	2.79	5.81(02)	0.82(02)	2.44(24)	0.13	6.2/6.2/6.0
DCC <sup>13</sup> CN	4–3 <sup>jl</sup>	33620.0314(04)	4.0	11.5 <sup>i</sup>	...	...	...	...	...	7.3/7.4/8.5
DCC <sup>13</sup> CN	5–4 <sup>j</sup>	42024.9652(06)	6.1	14.6 <sup>i</sup>	3.93	5.85(01)	0.71(02)	2.98(30)	0.13	6.2/6.2/6.0
DCCC <sup>15</sup> N	4–3	32802.9527(12)	3.9	4.00	1.08	5.86(03)	0.61(06)	0.70(07)	0.10	8.0
DCCC <sup>15</sup> N	5–4	41003.6144(15)	5.9	5.00	1.51	5.91(02)	0.71(06)	1.14(11)	0.12	6.3
DCCC <sup>15</sup> N	6–5	49204.2250(18)	8.3	6.00	1.19	5.88(08)	0.69(21)	0.88(09)	0.33	5.5
H <sup>13</sup> C <sup>13</sup> CCN	4–3 <sup>g</sup>	35137.0295(28)	4.2	2.86	0.39	5.80(16)	0.58(29)	0.24(02)	0.12	7.0
H <sup>13</sup> C <sup>13</sup> CCN	4–3 <sup>h</sup>	35137.1406(28)	4.2	8.64 <sup>i</sup>	1.60	5.73(03)	0.90(10)	1.53(15)	0.12	7.1/7.9
H <sup>13</sup> C <sup>13</sup> CCN	5–4 <sup>j</sup>	43921.3068(34)	6.3	14.6 <sup>i</sup>	1.97	5.74(03)	0.90(07)	1.90(19)	0.17	6.0/5.9/5.8
H <sup>13</sup> CC <sup>13</sup> CN	4–3 <sup>g</sup>	35110.0747(05)	4.2	2.86	0.50	5.57(32)	1.13(58)	0.61(06)	0.10	7.0
H <sup>13</sup> CC <sup>13</sup> CN	4–3 <sup>h</sup>	35110.1857(05)	4.2	8.64 <sup>i</sup>	1.73	5.70(04)	0.72(08)	1.32(13)	0.10	7.1/7.9
H <sup>13</sup> CC <sup>13</sup> CN	5–4 <sup>j</sup>	43887.6131(06)	6.3	14.6 <sup>i</sup>	2.54	5.78(02)	0.98(06)	2.66(26)	0.18	6.0/5.9/5.8
HC <sup>13</sup> C <sup>13</sup> CN	4–3 <sup>g</sup>	36082.3614(07)	4.3	2.86	0.74	5.70(07)	0.60(10)	0.47(05)	0.10	6.8
HC <sup>13</sup> C <sup>13</sup> CN	4–3 <sup>h</sup>	36082.4724(07)	4.3	8.64 <sup>i</sup>	2.23	5.76(04)	0.70(08)	1.66(17)	0.10	6.8/7.6
HC <sup>13</sup> C <sup>13</sup> CN	5–4 <sup>j</sup>	45102.9659(08)	6.5	14.6 <sup>i</sup>	2.90	5.76(02)	0.75(02)	2.32(23)	0.18	5.8/5.8/5.6
HCC <sup>13</sup> C <sup>15</sup> N	4–3	35205.8007(04)	4.2	4.00	1.35	5.76(03)	0.79(07)	1.13(11)	0.10	7.3
HCC <sup>13</sup> C <sup>15</sup> N	5–4	44007.1592(04)	6.3	5.00	1.28	5.65(05)	0.78(14)	1.07(11)	0.21	5.9
HC <sup>13</sup> CC <sup>15</sup> N	4–3	35173.1533(10)	4.2	4.00	0.99	5.84(04)	0.73(09)	0.76(07)	0.11	7.3
HC <sup>13</sup> CC <sup>15</sup> N	5–4 <sup>m</sup>	43966.3500(10)	6.3	5.00	1.36	5.89(02)	0.82(06)	1.19(12)	0.14	5.9

**Notes.** Values in parentheses are the uncertainty of the last significant figures. <sup>(a)</sup> Adopted rest frequencies. <sup>(b)</sup> Local standard of rest velocity of the emission for the adopted rest frequency (in km s<sup>-1</sup>). <sup>(c)</sup> Line width at half-intensity derived by fitting a Gaussian profile to the observed lines (in km s<sup>-1</sup>). <sup>(d)</sup> Integrated line intensity in mK km s<sup>-1</sup>. We assumed that the uncertainty is dominated by the calibration error of 10%. <sup>(e)</sup> The sensitivity of the data (root mean square error) has been derived from a baseline fit to each line in a velocity window from –10 to 20 km s<sup>-1</sup> (in mK). <sup>(f)</sup> Excitation temperature derived from the LVG modelling for each hyperfine transition. <sup>(g)</sup>  $F_u - F_l = 3 - 2$  component. <sup>(h)</sup> Weighted average of the  $F_u - F_l = 4 - 3$  and  $F_u - F_l = 5 - 4$  hyperfine components. <sup>(i)</sup> Sum of the line strengths of the hyperfine components that contribute to the line. <sup>(j)</sup> Weighted average of the three strongest hyperfine components. <sup>(k)</sup> Partially blended with an unidentified line. <sup>(l)</sup> Fully blended with C<sup>13</sup>CS. <sup>(m)</sup> Partially blended with HCCC<sup>13</sup>CCCN. The fit to the blended line was made as the sum of two independent lines with free parameters. One of the lines appears with the radial velocity of TMC-1, and we therefore assumed the parameters given for the fit of this line.

**Table A.3.** Observed line parameters for HCCCN in TMC-1.

Molecule	$J_u - J_l$	$F_u - F_l$	$\nu_{\text{rest}}^a$ (MHz)	$E_u/k_B$ (K)	$S_{ij}$	$T_A^*$ (K)	$v_{\text{LSR}}^b$ (km s <sup>-1</sup> )	$\Delta v^c$ (km s <sup>-1</sup> )	$\int T_A^* dv^d$ (K km s <sup>-1</sup> )	$\sigma^e$ (mK)	$T_{\text{ex}}^f$ (K)
HCCCN	4-3	4-4	36390.8876(05)	4.4	0.250	0.4410	5.79(01)	0.69(01)	0.3233(0323)	0.1	8.1
HCCCN	4-3	3-2	36392.2345(03)	4.4	2.857	1.9243	5.77(01)	0.75(01)	1.5322(1532)	0.1	8.0
HCCCN	4-3	4-3/5-4	<sup>g</sup> 36392.3455(03)	4.4	8.639 <sup>h</sup>	2.5952	5.76(01)	0.82(01)	2.5952(2595)	0.1	8.6/9.7
HCCCN	4-3	3-4	36392.7382(03)	4.4	0.004	0.0076	5.80(01)	0.71(01)	0.0058(0006)	0.1	7.4
HCCCN	4-3	3-3	36394.1777(06)	4.4	0.250	0.4404	5.78(01)	0.69(01)	0.3247(0325)	0.1	7.8
HCCCN	5-4	5-5	45488.8387(05)	6.5	0.200	0.3722	5.78(01)	0.59(01)	0.2338(0234)	0.2	7.4
HCCCN	5-4	4-3/5-4/6-5	<sup>g</sup> 45490.3063(05)	6.5	14.60 <sup>h</sup>	3.1585	5.80(01)	0.94(01)	3.1295(3129)	0.2	8.2/8.4/8.8
HCCCN	5-4	4-5	45490.6380(04)	6.5	0.002	0.0038	5.81(02)	0.50(03)	0.0020(0002)	0.2	6.7
HCCCN	5-4	4-4	45492.1101(06)	6.5	0.200	0.3712	5.80(01)	0.60(01)	0.2351(0235)	0.2	7.6
HCCCN	8-7	8-8	72782.2941(07)	15.7	0.125	0.2634	5.80(01)	0.50(01)	0.1413(0141)	4.1	7.4
HCCCN	8-7	7-6/8-7/9-8	<sup>g</sup> 72783.8171(06)	15.7	23.75 <sup>h</sup>	4.5540	5.78(01)	0.60(01)	2.9206(2921)	4.1	7.9/8.0/8.2
HCCCN	8-7	7-7	72785.5455(08)	15.7	0.125	0.1990	5.79(01)	0.52(01)	0.1102(0110)	4.1	7.4
HCCCN	9-8	9-9	81879.9284(08)	19.6	0.111	0.1735	5.81(01)	0.47(01)	0.0866(0087)	2.9	6.6
HCCCN	9-8	8-7/9-8/10-9	<sup>g</sup> 81881.4617(07)	19.6	26.78 <sup>h</sup>	4.3344	5.78(01)	0.53(01)	2.4576(2457)	2.9	7.1/7.2/7.3
HCCCN	9-8	8-8	81883.1771(08)	19.6	0.111	0.1333	5.79(01)	0.45(01)	0.0643(0064)	2.9	6.7
HCCCN	10-9	10-10	90977.4469(09)	24.0	0.100	0.0890	5.83(01)	0.46(01)	0.0436(0043)	2.7	5.8
HCCCN	10-9	9-8/10-9/11-10	<sup>g</sup> 90978.9886(08)	24.0	29.80 <sup>h</sup>	3.4147	5.81(01)	0.51(01)	1.8423(1842)	2.7	6.1/6.3/6.4
HCCCN	10-9	9-9	90980.6938(09)	24.0	0.100	0.0690	5.85(01)	0.42(01)	0.0312(0031)	2.7	5.8
HCCCN	11-10	11-11	100074.8364(09)	28.8	0.091	0.0331	5.85(01)	0.42(01)	0.0147(0015)	1.1	5.0
HCCCN	11-10	10-9/11-10/12-11	<sup>g</sup> 100076.3849(08)	28.8	32.82 <sup>h</sup>	2.2851	5.81(01)	0.49(01)	1.1864(1186)	1.1	5.3/5.4/5.4
HCCCN	11-10	10-10	100078.0818(10)	28.8	0.091	0.0241	5.84(01)	0.42(02)	0.0107(0011)	1.1	5.0
HCCCN	12-11	12-12	109172.0832(10)	34.1	0.083	0.0103	5.84(05)	0.25(13)	0.0027(0011)	4.4	4.5
HCCCN	12-11	11-10/12-11/13-12	<sup>g</sup> 109173.6375(10)	34.1	35.83 <sup>h</sup>	1.4581	5.83(01)	0.46(01)	0.7225(0722)	4.4	4.9/4.8/4.8
HCCCN	12-11	11-11	109175.3275(10)	34.1	0.083	0.0120	5.81(06)	0.19(12)	0.0025(0011)	4.4	4.6

**Notes.** Values in parentheses are the uncertainty of the last significant figures. <sup>(a)</sup> Adopted rest frequencies. <sup>(b)</sup> Local standard of rest velocity of the emission for the adopted rest frequency (in km s<sup>-1</sup>). <sup>(c)</sup> Line width at half-intensity derived by fitting a Gaussian profile to the observed lines (in km s<sup>-1</sup>). <sup>(d)</sup> Integrated line intensity in K km s<sup>-1</sup>; we assumed that the uncertainty is dominated by the calibration error of 10%. <sup>(e)</sup> The sensitivity of the data (root mean square error) has been derived from a baseline fit to each line in a velocity window from -15 to 25 km s<sup>-1</sup> (in mK). <sup>(f)</sup> Excitation temperature derived from the LVG modelling for each hyperfine transition. The density of the model is different for the lines at 7 mm ( $n(\text{H}_2) = 1 \times 10^4 \text{ cm}^{-3}$ ) and those at 3 mm ( $n(\text{H}_2) = 2 \times 10^4 \text{ cm}^{-3}$ ), see Sect. 3.1. <sup>(g)</sup> Weighted average of the involved hyperfine components. <sup>(h)</sup> Sum of the line strengths of the hyperfine components that contribute to the line.

**Table A.4.** Observed line parameters for singly substituted isotopologues of HCCCN in TMC-1.

Molecule	$J_u - J_l$	$F_u - F_l$	$\nu_{\text{rest}}^a$ (MHz)	$E_u/k_B$ (K)	$S_{ij}$	$T_A^*$ (K)	$v_{\text{LSR}}^b$ (km s <sup>-1</sup> )	$\Delta v^c$ (km s <sup>-1</sup> )	$\int T_A^* dv^d$ (K km s <sup>-1</sup> )	$\sigma^e$ (mK)	$T_{\text{ex}}^f$ (K)
DCCCN	4-3	4-4	33771.0873(03)	4.1	0.25	0.00715	5.82(1)	0.75(01)	0.0057(006)	0.09	6.6
DCCCN	4-3	3-2	33772.4373(03)	4.1	2.86	0.08011	5.71(1)	0.91(01)	0.0775(078)	0.09	7.3
DCCCN	4-3	4-3/5-4	<sup>g</sup> 33772.5500(03)	4.1	8.64 <sup>h</sup>	0.21635	5.80(1)	0.81(01)	0.1861(186)	0.09	7.5/8.5
DCCCN	4-3	3-3	33774.3772(03)	4.1	0.25	0.00470	5.84(1)	0.76(02)	0.0038(004)	0.09	6.8
DCCCN	5-4	5-5	42214.1049(04)	6.1	0.20	0.00546	5.81(1)	0.62(02)	0.0036(004)	0.12	5.4
DCCCN	5-4	4-3/5-4/6-5	<sup>g</sup> 42215.5779(03)	6.1	14.6 <sup>h</sup>	0.28307	5.80(1)	0.82(01)	0.2482(248)	0.12	6.3/6.3/6.2
DCCCN	5-4	4-4	42217.3762(04)	6.1	0.20	0.00530	5.83(1)	0.60(01)	0.0034(003)	0.12	6.0
DCCCN	9-8	8-7/9-8/10-9	<sup>g</sup> 75987.1367(06)	18.2	26.8 <sup>h</sup>	0.18741	5.83(1)	0.53(01)	0.1054(105)	2.80	4.6/4.6/4.5
DCCCN	10-9	9-8/10-9/11-10	<sup>g</sup> 84429.8088(07)	22.3	29.8 <sup>h</sup>	0.09951	5.83(1)	0.53(01)	0.0562(056)	0.81	4.5/4.5/4.5
DCCCN	11-10	10-9/11-10/12-11	<sup>g</sup> 92872.3725(07)	26.7	32.8 <sup>h</sup>	0.04898	5.85(1)	0.49(01)	0.0253(025)	0.92	4.6/4.6/4.6
DCCCN	12-11	11-10/12-11/13-12	<sup>g</sup> 101314.8168(08)	31.6	35.8 <sup>h</sup>	0.01870	5.84(2)	0.42(04)	0.0084(008)	2.04	4.6/4.6/4.6
DCCCN	13-12	12-11/13-12/14-13	<sup>g</sup> 109757.1310(08)	36.8	38.8 <sup>h</sup>	0.02084	5.82(4)	0.37(08)	0.0082(016)	4.89	4.7/4.7/4.7
H <sup>13</sup> CCCN	4-3	4-4	35265.9791(49)	4.2	0.25	0.00437	5.95(2)	0.62(04)	0.0031(003)	0.14	6.2
H <sup>13</sup> CCCN	4-3	3-2	35267.3117(07)	4.2	2.86	0.05278	5.79(1)	0.72(01)	0.0402(040)	0.14	7.0
H <sup>13</sup> CCCN	4-3	4-3/5-4	<sup>g</sup> 35267.4215(06)	4.2	8.64 <sup>h</sup>	0.14143	5.77(1)	0.76(01)	0.1148(115)	0.14	7.1/7.9
H <sup>13</sup> CCCN	4-3	3-3	35269.2342(62)	4.2	0.25	0.00482	5.63(1)	0.71(02)	0.0036(004)	0.14	6.5
H <sup>13</sup> CCCN	5-4	5-5	44082.7057(50)	6.3	0.20	0.00367	5.91(2)	0.65(04)	0.0026(003)	0.21	5.1
H <sup>13</sup> CCCN	5-4	4-3/5-4/6-5	<sup>g</sup> 44084.1577(08)	6.3	14.6 <sup>h</sup>	0.17323	5.78(1)	0.79(01)	0.1456(146)	0.21	6.0/6.0/5.8
H <sup>13</sup> CCCN	5-4	4-4	44085.9423(61)	6.3	0.20	0.00306	5.69(2)	0.55(04)	0.0018(002)	0.21	5.6
H <sup>13</sup> CCCN	9-8	8-7/9-8/10-9	<sup>g</sup> 79350.4624(13)	19.0	26.8 <sup>h</sup>	0.08837	5.81(1)	0.50(01)	0.0469(047)	2.01	4.5/4.5/4.4
H <sup>13</sup> CCCN	10-9	9-8/10-9/11-10	<sup>g</sup> 88166.7930(14)	23.3	29.8 <sup>h</sup>	0.04218	5.80(1)	0.44(02)	0.0195(020)	2.55	4.5/4.5/4.5
H <sup>13</sup> CCCN	11-10	10-9/11-10/12-11	<sup>g</sup> 96983.0010(16)	27.9	32.8 <sup>h</sup>	0.01794	5.82(1)	0.54(02)	0.0103(010)	0.64	4.6/4.6/4.5
H <sup>13</sup> CCCN	12-11	11-10/12-11/13-12	<sup>g</sup> 105799.0742(17)	33.0	35.8 <sup>h</sup>	0.00661	5.59(7)	0.26(13)	0.0018(009)	3.31	4.6/4.6/4.6
H <sup>13</sup> CCCN	13-12	12-11/13-12/14-13	<sup>g</sup> 114615.0008(19)	38.5	38.8 <sup>h</sup>	<sup>i</sup> ...	...	...	...	7.04	4.7/4.7/4.7
HC <sup>13</sup> CCN	4-3	4-4	36236.5139(53)	4.3	0.25	0.00508	5.87(1)	0.71(02)	0.0038(004)	0.11	6.1
HC <sup>13</sup> CCN	4-3	3-2	36237.8536(07)	4.3	2.86	0.05919	5.76(1)	0.74(01)	0.0467(047)	0.11	6.8
HC <sup>13</sup> CCN	4-3	4-3/5-4	<sup>g</sup> 36237.9641(07)	4.3	8.64 <sup>h</sup>	0.15201	5.74(1)	0.70(01)	0.1132(113)	0.11	6.8/7.6
HC <sup>13</sup> CCN	4-3	3-3	36239.7865(68)	4.3	0.25	0.00499	5.72(1)	0.67(02)	0.0036(004)	0.11	6.3
HC <sup>13</sup> CCN	5-4	5-5	45295.8703(54)	6.5	0.20	0.00326	5.87(2)	0.53(04)	0.0018(002)	0.17	5.0
HC <sup>13</sup> CCN	5-4	4-3/5-4/6-5	<sup>g</sup> 45297.3301(08)	6.5	14.6 <sup>h</sup>	0.18974	5.78(1)	0.78(01)	0.1573(157)	0.17	5.8/5.8/5.7
HC <sup>13</sup> CCN	5-4	4-4	45299.1243(67)	6.5	0.20	0.00370	5.73(1)	0.55(02)	0.0022(002)	0.17	5.5
HC <sup>13</sup> CCN	8-7	7-6/8-7/9-8	<sup>g</sup> 72475.0586(13)	15.7	23.7 <sup>h</sup>	0.16345 <sup>j</sup>	5.80(2)	0.53(03)	0.0924(092)	3.51	4.5/4.5/4.5
HC <sup>13</sup> CCN	9-8	8-7/9-8/10-9	<sup>g</sup> 81534.1100(14)	19.6	26.8 <sup>h</sup>	0.07847	5.82(1)	0.56(01)	0.0465(046)	0.77	4.5/4.4/4.4
HC <sup>13</sup> CCN	10-9	9-8/10-9/11-10	<sup>g</sup> 90593.0444(15)	23.9	29.8 <sup>h</sup>	0.04196	5.83(1)	0.50(02)	0.0222(022)	1.73	4.5/4.5/4.4
HC <sup>13</sup> CCN	11-10	10-9/11-10/12-11	<sup>g</sup> 99651.8487(17)	28.7	32.8 <sup>h</sup>	0.01884	5.82(1)	0.59(02)	0.0191(019)	0.95	4.6/4.5/4.5
HC <sup>13</sup> CCN	12-11	11-10/12-11/13-12	<sup>g</sup> 108710.5101(18)	33.9	35.8 <sup>h</sup>	0.01088	5.89(8)	0.34(17)	0.0040(013)	3.70	4.6/4.6/4.6
HCC <sup>13</sup> CN	4-3	4-4	36240.0103(24)	4.3	0.25	0.00766	5.83(1)	0.70(01)	0.0057(006)	0.12	6.1
HCC <sup>13</sup> CN	4-3	3-2	36241.3514(07)	4.3	2.86	0.08741	5.74(1)	0.74(01)	0.0689(069)	0.12	6.8
HCC <sup>13</sup> CN	4-3	4-3/5-4	<sup>g</sup> 36241.4620(07)	4.3	8.64 <sup>h</sup>	0.22545	5.78(1)	0.79(01)	0.1899(190)	0.12	6.9/7.6
HCC <sup>13</sup> CN	4-3	3-3	36243.2863(30)	4.3	0.25	0.00791	5.72(1)	0.70(01)	0.0060(006)	0.12	6.3
HCC <sup>13</sup> CN	5-4	5-5	45300.2411(25)	6.5	0.20	0.00547	5.84(1)	0.62(02)	0.0036(004)	0.15	5.0
HCC <sup>13</sup> CN	5-4	4-3/5-4/6-5	<sup>g</sup> 45301.7024(09)	6.5	14.6 <sup>h</sup>	0.27014	5.76(1)	0.78(01)	0.2249(225)	0.15	5.8/5.8/5.7
HCC <sup>13</sup> CN	5-4	4-4	45303.4985(30)	6.5	0.20	0.00534	5.74(1)	0.60(03)	0.0034(003)	0.15	5.5
HCC <sup>13</sup> CN	8-7	7-6/8-7/9-8	<sup>g</sup> 72482.0540(14)	15.7	23.7 <sup>h</sup>	0.22458 <sup>j</sup>	5.77(2)	0.57(03)	0.1368(137)	4.22	4.5/4.5/4.5
HCC <sup>13</sup> CN	9-8	8-7/9-8/10-9	<sup>g</sup> 81541.9798(15)	19.6	26.8 <sup>h</sup>	0.11192	5.80(1)	0.55(01)	0.0654(065)	0.82	4.5/4.4/4.4
HCC <sup>13</sup> CN	10-9	9-8/10-9/11-10	<sup>g</sup> 90601.7884(16)	23.9	29.8 <sup>h</sup>	0.06330	5.80(1)	0.49(01)	0.0328(033)	1.54	4.5/4.5/4.4
HCC <sup>13</sup> CN	11-10	10-9/11-10/12-11	<sup>g</sup> 99661.4670(18)	28.7	32.8 <sup>h</sup>	0.02553	5.77(1)	0.50(02)	0.0135(014)	0.93	4.6/4.5/4.5
HCC <sup>13</sup> CN	12-11	11-10/12-11/13-12	<sup>g</sup> 108721.0025(19)	33.9	35.8 <sup>h</sup>	0.01105 <sup>j</sup>	5.80(7)	0.49(17)	0.0058(015)	3.61	4.6/4.6/4.6
HCCC <sup>15</sup> N	4-3		35333.8879(07)	4.2	4.00	0.07884	5.76(1)	0.68(01)	0.0573(057)	0.12	7.3
HCCC <sup>15</sup> N	5-4		44167.2678(09)	6.4	5.00	0.08333	5.77(1)	0.60(01)	0.0532(053)	0.16	5.9
HCCC <sup>15</sup> N	9-8		79500.0510(15)	19.1	9.00	0.02823	5.75(2)	0.51(04)	0.0154(015)	2.05	4.5
HCCC <sup>15</sup> N	10-9		88333.0013(17)	23.3	10.0	0.01511	5.75(2)	0.39(06)	0.0063(008)	2.12	4.5
HCCC <sup>15</sup> N	11-10		97165.8288(19)	28.0	11.0	0.00537	5.74(4)	0.39(08)	0.0022(004)	1.11	4.6
HCCC <sup>15</sup> N	12-11		105998.5213(20)	33.1	12.0	<sup>i</sup> ...	...	...	...	3.59	4.6
HCCC <sup>15</sup> N	13-12		114831.0666(22)	38.6	13.0	<sup>i</sup> ...	...	...	...	7.22	4.9

**Notes.** Values in parentheses are the uncertainty of the last significant figures. <sup>(a)</sup> Adopted rest frequencies. <sup>(b)</sup> Local standard of rest velocity of the emission for the adopted rest frequency (in km s<sup>-1</sup>). <sup>(c)</sup> Line width at half-intensity derived by fitting a Gaussian profile to the observed lines (in km s<sup>-1</sup>). <sup>(d)</sup> Integrated line intensity in mK km s<sup>-1</sup>. We assumed that the uncertainty is dominated by the calibration error of 10%. <sup>(e)</sup> The sensitivity of the data (root mean square error) has been derived from a baseline fit to each line in a velocity window from -15 to 25 km s<sup>-1</sup> (in mK). <sup>(f)</sup> Excitation temperature derived from the LVG modelling for each hyperfine transition. <sup>(g)</sup> Weighted average of the involved hyperfine components. <sup>(h)</sup> Sum of the line strengths of the hyperfine components that contribute to the line. <sup>(i)</sup> Below the detection limit. <sup>(j)</sup> Partially blended with a negative feature produced in the data folding of the frequency-switching observation procedure.

**Table A.5.** Column densities ( $N$ ) and derived isotopic ratios for the HC<sub>3</sub>N isotopologues towards TMC-1 (CP).

Species	$N$ (cm <sup>-2</sup> )	$N$ (cm <sup>-2</sup> )	D/H	C/ <sup>13</sup> C	Isotopic ratios <sup>a</sup>			<sup>13</sup> C/ <sup>15</sup> N
	(LVG)	(LTE)			N/ <sup>15</sup> N	D/ <sup>13</sup> C	D/ <sup>15</sup> N	
HCCCN	$1.90(03) \times 10^{14}$	$3.62(75) \times 10^{14}$	...	...	...	...	...	...
DCCCN	$3.30(04) \times 10^{12}$	$5.93(29) \times 10^{12}$	0.0174(3) <sup>b</sup>	...	...	...	...	...
H <sup>13</sup> CCCN	$1.80(06) \times 10^{12}$	$5.15(22) \times 10^{12}$	...	106(4) <sup>b</sup>	...	1.83(6) <sup>g</sup>	...	3.000(7) <sup>f</sup>
HC <sup>13</sup> CCN	$2.00(04) \times 10^{12}$	$3.75(17) \times 10^{12}$	...	95(2) <sup>b</sup>	...	1.65(4) <sup>g</sup>	...	3.333(7) <sup>f</sup>
HCC <sup>13</sup> CN	$2.80(04) \times 10^{12}$	$6.46(08) \times 10^{12}$	...	69(1) <sup>b</sup>	...	1.18(2) <sup>g</sup>	...	4.667(8) <sup>f</sup>
HCCC <sup>15</sup> N	$0.60(01) \times 10^{12}$	$1.53(03) \times 10^{12}$	...	...	317(4) <sup>b</sup>	...	5.50(7) <sup>g</sup>	...
D <sup>13</sup> CCCN	$3.20(12) \times 10^{10}$	...	0.0178(9) <sup>c</sup>	103(4) <sup>g</sup>	...	1.7(2) <sup>h</sup> ; 1.4(1) <sup>i</sup>	...	3.2(3) <sup>p</sup>
DC <sup>13</sup> CCN	$2.50(11) \times 10^{10}$	...	0.0125(6) <sup>d</sup>	132(6) <sup>g</sup>	...	1.3(1) <sup>h</sup> ; 1.00(8) <sup>j</sup>	...	2.5(2) <sup>p</sup>
DCC <sup>13</sup> CN	$3.50(12) \times 10^{10}$	...	0.0125(5) <sup>e</sup>	94(3) <sup>g</sup>	...	1.5(1) <sup>i</sup> ; 1.4(1) <sup>j</sup>	...	3.5(3) <sup>p</sup>
DCCC <sup>15</sup> N	$1.00(09) \times 10^{10}$	...	0.017(2) <sup>f</sup>	...	330(31) <sup>g</sup>	0.9(2) <sup>k</sup> ; 1.2(2) <sup>l</sup>	...	...
H <sup>13</sup> C <sup>13</sup> CCN	$1.90(16) \times 10^{10}$	...	...	95(9) <sup>c</sup> ; 105(9) <sup>d</sup>	...	1.7(2) <sup>m</sup> ; 1.3(1) <sup>n</sup>	...	2.4(3) <sup>l</sup>
H <sup>13</sup> CC <sup>13</sup> CN	$2.30(16) \times 10^{10}$	...	...	78(6) <sup>c</sup> ; 123(9) <sup>e</sup>	...	1.4(1) <sup>m</sup> ; 1.5(1) <sup>o</sup>	...	2.1(4) <sup>k</sup>
HC <sup>13</sup> C <sup>13</sup> CN	$2.50(16) \times 10^{10}$	...	...	80(5) <sup>d</sup> ; 112(7) <sup>e</sup>	...	1.08(8) <sup>n</sup> ; 1.4(1) <sup>o</sup>	...	2.3(4) <sup>k</sup> ; 3.1(4) <sup>l</sup>
HCC <sup>13</sup> C <sup>15</sup> N	$1.10(18) \times 10^{10}$	...	...	55(9) <sup>f</sup>	255(42) <sup>e</sup>	0.9(2) <sup>p</sup>	3.2(5) <sup>o</sup>	...
HC <sup>13</sup> CC <sup>15</sup> N	$0.80(09) \times 10^{10}$	...	...	75(8) <sup>f</sup>	250(28) <sup>d</sup>	1.3(2) <sup>p</sup>	3.1(4) <sup>n</sup>	...

**Notes.** Values in parentheses are the uncertainty of the last significant figures. <sup>(a)</sup> Column density ratios calculated using the derived LVG column densities. <sup>(b)</sup> Using HCCCN. <sup>(c)</sup> Using H<sup>13</sup>CCCN. <sup>(d)</sup> Using HC<sup>13</sup>CCN. <sup>(e)</sup> Using HCC<sup>13</sup>CN. <sup>(f)</sup> Using HCCC<sup>15</sup>N. <sup>(g)</sup> Using DCCCN. <sup>(h)</sup> Using H<sup>13</sup>C<sup>13</sup>CCN. <sup>(i)</sup> Using H<sup>13</sup>CC<sup>13</sup>CN. <sup>(j)</sup> Using HC<sup>13</sup>C<sup>13</sup>CN. <sup>(k)</sup> Using HCC<sup>13</sup>C<sup>15</sup>N. <sup>(l)</sup> Using HC<sup>13</sup>CC<sup>15</sup>N. <sup>(m)</sup> Using D<sup>13</sup>CCCN. <sup>(n)</sup> Using DC<sup>13</sup>CCN. <sup>(o)</sup> Using DCC<sup>13</sup>CN. <sup>(p)</sup> Using DCCC<sup>15</sup>N.